

Surpassing light inhomogeneities in structured-illumination microscopy with FlexSIM

Emmanuel Soubies¹  | Alejandro Nogueron² | Florence Pelletier³ |
Thomas Mangeat⁴ | Christophe Leterrier³ | Michael Unser² | Daniel Sage²

¹IRIT, Université de Toulouse, CNRS, Toulouse, France

²Biomedical Imaging Group, EPFL, Lausanne, Switzerland

³CNRS, INP, NeuroCyto Lab, Aix Marseille Université, Marseille, France

⁴LITC Core Facility, Centre de Biologie Intégrative, Université de Toulouse, CNRS, Toulouse, France

Correspondence

Emmanuel Soubies, IRIT, Université de Toulouse, CNRS, Toulouse, France.
Email: emmanuel.soubies@cnrs.fr

Funding information

ANR Micro-Blind; Agence Nationale de la Recherche, Grant/Award Numbers: ANR-21-CE48-0008, ANR-11-LABX-0040; A*MIDEX, Grant/Award Number: AMX-19-IET-002

Abstract

Super-resolution structured-illumination microscopy (SIM) is a powerful technique that allows one to surpass the diffraction limit by up to a factor two. Yet, its practical use is hampered by its sensitivity to imaging conditions which makes it prone to reconstruction artefacts. In this work, we present FlexSIM, a *flexible* SIM reconstruction method capable to handle highly challenging data. Specifically, we demonstrate the ability of FlexSIM to deal with the distortion of patterns, the high level of noise encountered in live imaging, as well as out-of-focus fluorescence. Moreover, we show that FlexSIM achieves state-of-the-art performance over a variety of open SIM datasets.

KEYWORDS

artefact reduction, computational imaging, image reconstruction, patterns estimation, super-resolution, structured-illumination microscopy

1 | INTRODUCTION

Since the seminal works of Heintzmann, Cremer¹ and Gustafsson,² super-resolution structured-illumination microscopy (SIM) has become increasingly popular.^{3–7} Among super-resolution fluorescence microscopy techniques,^{8–10} it is one of those that offer the best trade-off between spatial and temporal resolution.^{11–13} Moreover, it does not require specific sample preparations, offers high photon efficiency, and supports multicolour imaging.^{3,14,15}

SIM is a prime example of *computational microscopy* that combines optics and numerical reconstruction so as to surpass the diffraction limit. Specifically, a set of structured illuminations is exploited to shift high-frequency

components of the imaged sample within the bandpass of the optical system. Then, through dedicated algorithms, this high-frequency information is extracted from acquired data and used to generate an image with extended resolution. From a numerical standpoint, the importance and popularity of SIM can be measured by the growing number of reconstruction software packages.¹⁶ These include, among open-source packages, SIMToolbox¹⁷; FairSIM¹⁸; OpenSIM¹⁹; Hessian-SIM²⁰; DL-SIM²¹; HiFi-SIM²²; ML-SIM²³; JSFR-SIM²⁴; Direct-SIM²⁵; rDL-SIM²⁶; or Open3DSIM.²⁷

In conventional SIM, sinusoidal illumination patterns are used, which allows one to improve the resolution of widefield microscopy by up to a factor two.^{1,2} Yet, several extensions of this conventional SIM setup have

This is an open access article under the terms of the [Creative Commons Attribution-NonCommercial-NoDerivs](https://creativecommons.org/licenses/by-nc-nd/4.0/) License, which permits use and distribution in any medium, provided the original work is properly cited, the use is non-commercial and no modifications or adaptations are made.

© 2024 The Author(s). *Journal of Microscopy* published by John Wiley & Sons Ltd on behalf of Royal Microscopical Society.

been proposed. They undertake to improve the resolution even further, to image thick samples, to reduce acquisition time, to simplify acquisition protocols, or to reduce background fluorescence.^{4–6} For instance, a resolution improvement beyond a factor two is theoretically achievable if the fluorescence emission can be made to depend nonlinearly on the illumination.^{28–31} Moreover, it has been shown that the use of random (speckle) illuminations improves the imaging of thick samples.^{32–35} In another vein, SIM has been combined with total internal reflection fluorescence (TIRF)^{36–38} or grazing incidence³⁹ illuminations. These limit the excitation to a few hundred nanometres above the coverslip, which strongly reduces out-of-focus fluorescence.

Unfortunately, SIM is particularly prone to reconstruction artefacts, which hinders its practical use. This has led some researchers to characterise and classify typical SIM artefacts.^{40–42} Other researchers have dedicated their work to the development of (i) detailed protocols for sample preparation⁴³ and system calibration^{40,44}; (ii) numerical tools to assess image quality⁴⁵; and (iii) guidelines to best take advantage of reconstruction software packages.^{38,40–42}

The quest for artefact-free SIM reconstruction is currently a very active area of research, as evidenced by the recent surge in numerical strategies such as the shaping of the reconstruction point-spread function (PSF) or optical transfer function (OTF) into an ideal form to reduce commonly seen artefacts,^{22,46} the deployment of rolling reconstructions to mitigate motion artefacts in life imaging,²⁰ the estimation and filtering of background fluorescence,^{47–49} the use of blind-reconstruction approaches,^{50–52} as well as the control of noise to remove structured-noise artefacts.⁵³ Finally, it is worth mentioning that deep neural networks have also been designed and trained to reduce artefacts in SIM reconstructions.^{54,55}

This situation (along with the difficulties we experienced ourselves upon striving to significantly reduce reconstruction artefacts for challenging TIRF-SIM data using existing methods) motivated the development of FlexSIM. The promise of FlexSIM, for *flexible* SIM reconstruction, is to provide reliable SIM reconstructions for a variety of SIM data, going from ‘ideal’ ones acquired under standardised protocols and configurations, to ones obtained under more challenging settings and more prone to reconstruction artefacts.

2 | MATERIALS AND METHODS

2.1 | Foundations of FlexSIM

FlexSIM builds upon three pillars, highlighted in Figure 1.

- (1) *Improved modelling.* We propose the use of a more realistic model to represent the experimental illumination patterns. Specifically, we consider

$$w = \underline{w} + a \cos(\mathbf{k}^t \cdot + \phi), \quad (1)$$

where \underline{w} represents a low-frequency component (to be estimated from data) that refines the simple model of a purely sinusoidal SIM pattern with amplitude a , wave vector \mathbf{k} , and phase ϕ . This refinement turned out to be essential to treat challenging TIRF-SIM data, as shown in Figure 2. Then, reconstruction is performed using a weighted-least-squares data-fidelity term that allows us to account for both out-of-focus signal (similarly to OTF attenuation in standard Wiener-based reconstruction) and shot noise.

- (2) *Auto-calibration of patterns.* In FlexSIM, pattern phases and orientations are estimated through the optimisation of the new criterion in (4), which we tackle in a two-step procedure. The criterion is first evaluated on a grid of candidate parameters over which optimal ones are selected. This grid-based initialisation, which can be efficiently performed through cross-correlation computations, somehow recovers the widespread approach of the seminal work,² without the need to unmix frequency components. The proposed approach can thus work with uneven phase shifts. This initial estimation is then refined (off-the-grid) through a gradient descent over the proposed criterion. Regarding the estimation of the low-frequency component \underline{w} , we proposed in FlexSIM an efficient method to estimate it (one per SIM image) directly from the data (see Section 2.2.4).
- (3) *Advanced reconstruction.* Lastly, FlexSIM benefits from the GlobalBioIm framework⁵⁶ which offers a variety of regularisers and optimisation algorithms. By default, first-order Tikhonov, smoothed total-variation and good-roughness regularisers are proposed in FlexSIM. Optimisation is performed with a quasi-Newton approach.

We provide in Sections 2.2 and 2.3 the methodological details behind each step of the FlexSIM pipeline.

Notations

We write vectors as bold lowercase letters (e.g., \mathbf{x} , \mathbf{k}) and their transpose as \mathbf{x}^t , \mathbf{k}^t . The m th component of a vector $\mathbf{x} \in \mathbb{R}^M$ is x_m . We denote the Fourier transform of a function v (lowercase) by its uppercase counterpart V . The symbols $*$ and \odot stand for convolution and pointwise multiplication operations, respectively. The complex conjugate of $a \in \mathbb{C}$ is denoted \bar{a} . We denote by $\langle \cdot, \cdot \rangle$ the standard Hermitian inner product, the conjugation being applied to the first argument by convention.

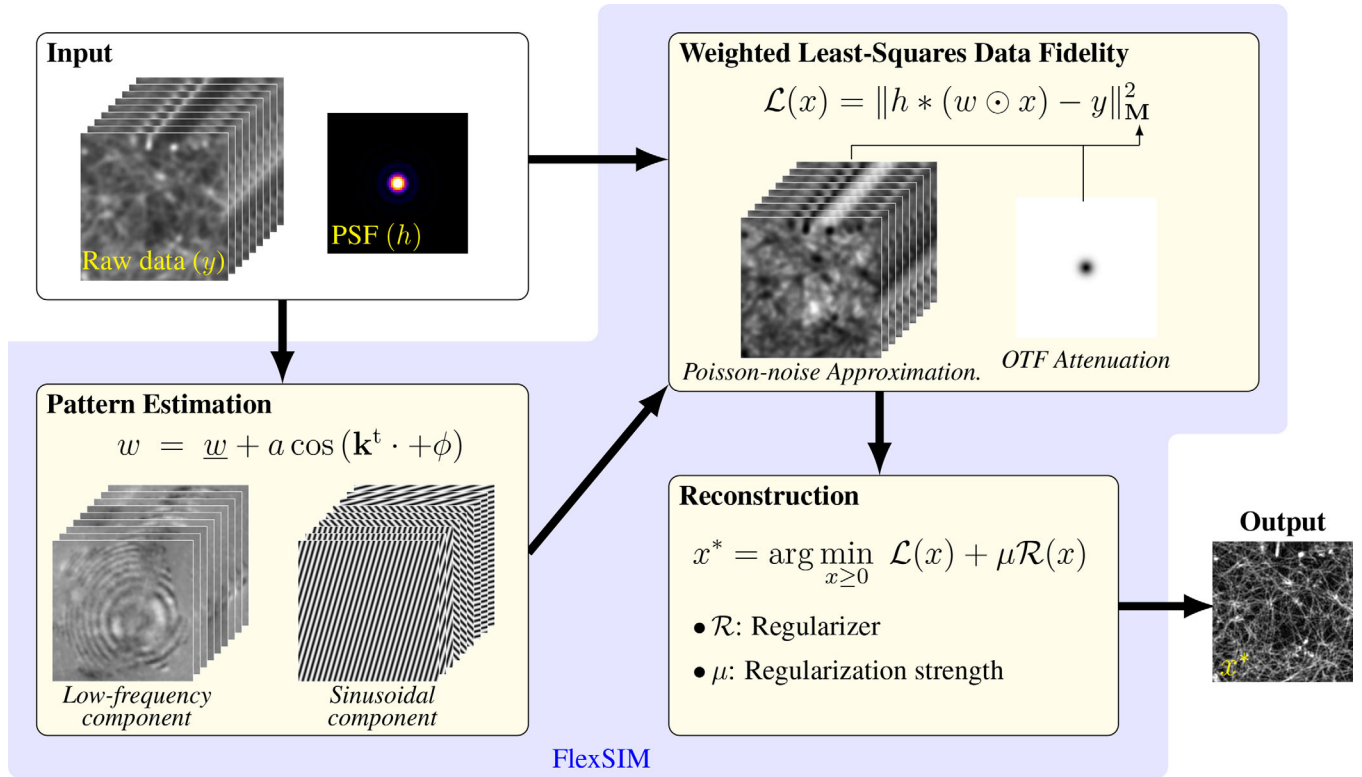


FIGURE 1 Flowchart of FlexSIM. In addition to the ideal sinusoidal illuminations, low-frequency pattern components w are estimated from raw data. For reconstruction, a weighted least-squares data-fidelity term is considered. The weighting operators \mathbf{M} are built so as to account for both out-of-focus signal (similarly to OTF attenuation) and shot-noise. Finally, reconstruction can be performed with a variety of regularisers \mathcal{R} and optimisation algorithms.

2.2 | Pattern estimation module

2.2.1 | The art of pattern estimation

An accurate pattern estimation is essential to limit reconstruction artefacts. The vast majority of existing approaches work under the assumption that the spatial phases shifts of patterns sharing the same orientation are regularly spaced within $[0, 2\pi]$. This allows for a simple separation of the Fourier components contained in the raw SIM images from the sole knowledge of relative phases. Then, the maximisation of the cross-correlation between these extracted Fourier components leads one to estimate the orientations of the patterns, as well as their frequencies and phase offsets.^{2,18,57} While this strategy proved to be very efficient to estimate pattern orientations and frequencies, it may not provide a sufficiently accurate estimation of phases. As such, several works have been dedicated to phase estimation, assuming that orientations and frequencies are known and that phases are not necessarily regularly spaced.^{58–61} Finally, there exist alternative approaches that exploit either Prony's annihilation property,⁶² or the low-rank nature⁶³ of SIM illuminations.

2.2.2 | Patterns estimation with FlexSIM

Let $\{w_m\}_{m=1}^M$ be M illumination patterns having the same orientation but different phases $\{\phi_m\}_{m=1}^M$. In conventional 2D-SIM, patterns are generated from the interference between two beams and are modelled as

$$w_m(\mathbf{x}) = 1 + a_m \cos(\mathbf{k}^t \mathbf{x} + \phi_m), \quad (2)$$

where $a_m > 0$ is the modulation contrast, $\mathbf{x} \in \mathbb{R}^2$ the spatial variable, and $\mathbf{k} \in \mathbb{R}^2$ the modulation light wave vector. The associated (noiseless) SIM data $\{v_m\}_{m=1}^M$ are then given by

$$\begin{aligned} v_m &= h * (w_m \odot u) \\ &= h * u + a_m h * (\cos(\mathbf{k}^t \cdot + \phi_m) \odot u), \end{aligned} \quad (3)$$

where u represents the sample and h the PSF of the optical system. In the sequel, we denote by $\tilde{v} = h * u$ the wide-field image, which we assume to be accessible. When the phases are equally spaced, we have that $\tilde{v} = \sum_{m=1}^M v_m$. Otherwise, the widefield image can be acquired together with the SIM stack.

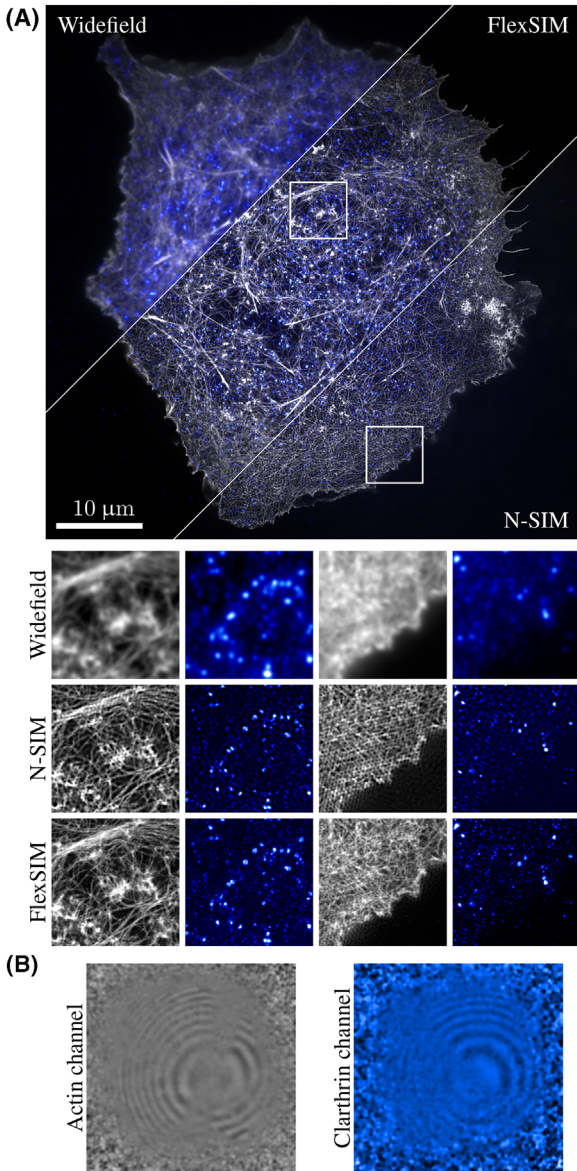


FIGURE 2 FlexSIM reconstruction of challenging TIRF-SIM data. Actin network (grey) and clathrin (blue) in COS-7 cells imaged using the Nikon N-SIM-S system in TIRF-SIM mode. Raw images are of size (1024×1024) and reconstructions are (2048×2048) . (A) Comparisons of reconstructions obtained with FlexSIM and the N-SIM software. (B) Low-frequency patterns components estimated by FlexSIM. Reconstructions of similar datasets are presented in Figures S7 and S8.

To drop the dependence on the sample u , which is unknown, we make the approximation that $u \approx \tilde{v}$. Then, pattern parameters can be estimated through the minimisation with respect to \mathbf{a} , $\boldsymbol{\phi}$, and \mathbf{k} of the criterion

$$\mathcal{J}(\mathbf{a}, \boldsymbol{\phi}, \mathbf{k}) = \sum_{m=1}^M \left\| a_m h * (\cos(\mathbf{k}^t \cdot + \phi_m) \odot \tilde{v}) - g * \tilde{v}_m \right\|_2^2, \quad (4)$$

where $\boldsymbol{\phi} \in [0, 2\pi)^M$, $\mathbf{a} \in \mathbb{R}_{>0}^M$, and $\tilde{v}_m = (v_m - \tilde{v})$ corresponds to the m th raw SIM data without the widefield

component. In practice, to account for scaling factors, we compute $\tilde{v}_m := (\alpha_m v_m - \tilde{v})$ for α_m that minimises the error $\|D \odot (\tilde{V} - \alpha_m \tilde{V}_m)\|_2^2$, that is $\alpha_m = \langle D \odot \tilde{V}, D \odot \tilde{V}_m \rangle / \|D \odot \tilde{V}_m\|_2^2$. Here, D is a mask that allows us to compute the error between low frequencies only (e.g., a disk in Fourier). Finally, g is a filter introduced to mitigate the effect of the approximation $u \approx \tilde{v}$. More precisely, the approximation $u \approx \tilde{v}$ amounts to consider (in first approximation) that we can commute the convolution and multiplication operators. This generates a mismatch error between the simplified model $a_m h * (\cos(\mathbf{k}^t \cdot + \phi_m) \odot \tilde{v})$ and the data \tilde{v}_m as illustrated in the third column of Figure S3. The role of g is thus to mitigate this mismatch (cf. last column of Figure S3). It is related to the idea of notch filtering used in other works.²²

The function \mathcal{J} is highly nonconvex, making its minimisation a challenging task. As such, we propose a two-step procedure.

1. *Grid-based initialisation.* The idea here is to consider an approximation of \mathcal{J} that can be efficiently evaluated on a grid $\mathcal{K} = \{\mathbf{k}_q\}_{q=1}^Q$ of candidate wave vectors, and then select $\mathbf{k}_{\text{init}} = \min_{\mathbf{k} \in \mathcal{K}} \mathcal{J}(\mathbf{k}) \in \mathcal{K}$. We refer the reader to *Supplementary Note 1* for a full derivation. Similar to standard pattern-estimation approaches,^{2,59} the proposed grid-based initialisation relies on cross-correlation computations. Yet, it does not require us to first unmix the frequency components. The advantage is that it can work with uneven phase shifts in a noniterative way. The main computational cost lies in the computation of M cross-correlation maps. In that respect, it has links with the method proposed in Ref. [60].
2. *Local off-the-grid refinement.* The goal here is to improve the initial estimation through a local optimisation of \mathcal{J} . This allows us to obtain an estimate of the wave vector that is not constrained to be on the grid \mathcal{K} used at initialisation. Moreover, the proposed local refinement deals with the exact function \mathcal{J} . It proceeds by alternating between a minimisation of \mathcal{J} with respect at first to $(\mathbf{a}, \boldsymbol{\phi})$, and then \mathbf{k} . For the minimisation over $(\mathbf{a}, \boldsymbol{\phi})$, we recast the problem as the resolution of $M(2 \times 2)$ systems of linear equations that can be solved efficiently. Regarding the minimisation of \mathcal{J} over \mathbf{k} , we derive a closed-form expression of the gradient and deploy gradient-descent steps. Full details are provided in *Supplementary Note 1*.

2.2.3 | Numerical validation

We report in Figure S4 a series of numerical experiments over simulated data. As expected, we observe that errors decrease when the level of noise decrease, that is when

the maximal expected number of photons (MEP) increases. For all noise levels, the wave vector is estimated with a precision that is beyond a tenth of pixel and reaches a hundredth of pixel for low noise levels. For the estimation of phases, errors vary from less than 10° for high noise levels to less than 1° when the noise decreases (Figure S4C). These are similar to the errors obtained with state-of-the-art methods.^{59–61}

An important outcome is that the same accuracy is reached with or without the assumption that the phases are equally spaced. However, challenging real data such as those acquired in a TIRF-SIM mode do benefit from the assumption that the phases are equally spaced.

Finally, let us comment on how oversampled data influence the quality of the cross-correlation map (initialisation step) (Figure S4B). As expected, pattern-estimation errors decrease as the oversampling increases. Yet, even with a 16-fold oversampling, the cross-correlation-based initialisation does not reach the accuracy obtained after our refinement step. This is especially true for MEP larger than 10, which corresponds to typical noise levels encountered in practice. This highlights the relevance of the proposed local refinement step.

Moreover, large oversampling factors significantly increase the memory usage and computational time. For instance, for the (512×512) image used in Figure S4, the cross-correlation computation with a 16-fold oversampling is six times slower than the two-step approach: initialisation (with twofold oversampling) plus local refinement (~ 30 s vs. ~ 5 s). As such, given that exceeding a twofold oversampling for the initialisation does not lead to a significant gain in the refinement step, the oversampling factor is fixed to 2 in FlexSIM.

2.2.4 | Estimation of pattern low-frequency component

An important feature of FlexSIM is that it allows us to consider patterns of the form

$$w_m(\mathbf{x}) = \underline{w}_m(\mathbf{x}) + a_m \cos(\mathbf{k}^t \mathbf{x} + \phi_m), \quad (5)$$

where \underline{w}_m is a low-frequency component. This model proved to be crucial to obtain meaningful reconstructions for the TIRF-SIM data of Figures 2, 3, and S6–S9.

Regarding the estimation of \underline{w}_m , we deploy a simple and fast method. It relies on the fact that, given a low pass filter f , we get from (3) and (5) that

$$\begin{aligned} f * v_m &\approx f * h * (\underline{w}_m \odot u) \\ &\approx \underline{w}_m \odot (f * h * u) = \underline{w}_m \odot (f * \tilde{v}), \end{aligned} \quad (6)$$

where we recall that \tilde{v} stands for the widefield image. From these approximations, we propose to use

$$\hat{\underline{w}}_m = (f * v_m) / (f * \tilde{v}) \quad (7)$$

as an estimate of \underline{w}_m (with pointwise division). This approach is illustrated in Figure S5.

2.3 | Image reconstruction module

2.3.1 | From direct wiener inversion to iterative reconstruction approaches

Most SIM reconstruction methods are variants of a direct Wiener inversion.² For standard sinusoidal illuminations, one can easily establish and solve a closed system of equations to unmix the Fourier components of SIM data and place them back to their right location in the Fourier domain. Then, a final Wiener filtering can be used to invert the effect of the OTF and limit the amplification of noise. More evolved deconvolution approaches, for instance those that account for Poisson noise, can also be used in this final step.⁶⁴ Alternatively, the consideration of a more general variational framework allows for the use of arbitrary (nonsinusoidal) illuminations,⁶⁵ a reduced number of images,⁶⁶ advanced regularisation terms,^{47,66–68} additional out-of-focus planes in the model,^{47,48} or blind reconstruction (i.e., joint pattern estimation and reconstruction).^{50,51}

2.3.2 | Image reconstruction with FlexSIM

We consider a variational reconstruction framework. Specifically, given P SIM raw images $\{\mathbf{y}_p \in \mathbb{R}^N\}_{p=1}^P$ composed of N pixels and associated with the (discretized) patterns $\{\mathbf{w}_p \in \mathbb{R}^N\}_{p=1}^P$, we compute the reconstructed image $\hat{\mathbf{u}} \in \mathbb{R}^{4N}$ (over a twice finer grid) as

$$\hat{\mathbf{u}} = \arg \min_{\mathbf{u} \geq 0} \sum_{p=1}^P \frac{1}{2} \|\mathbf{S}\mathbf{H}\mathbf{W}_p \mathbf{u} - \mathbf{y}_p\|_{\mathbf{M}_p}^2 + \mu \mathcal{R}(\mathbf{u}), \quad (8)$$

where $\mathbf{S} \in \mathbb{R}^{N \times 4N}$ is a twofold (in each dimension) down-sampling operator, $\mathbf{H} \in \mathbb{R}^{4N \times 4N}$ a convolution operator defined from the system PSF, and $\mathbf{W}_p = \mathbf{diag}(\mathbf{w}_p)$. Data fidelity is enforced using the ‘weighted’ L_2 -norm $\|\cdot\|_{\mathbf{M}_p}^2 = \langle \mathbf{M}_p \cdot, \cdot \rangle$, where $\mathbf{M}_p \in \mathbb{R}^{N \times N}$ is defined so as to account for Poisson noise and background/out-of-focus fluorescence (details hereafter). Finally, \mathcal{R} is a regularisation term and $\mu > 0$ a parameter that controls the trade-off between data fidelity and regularisation.

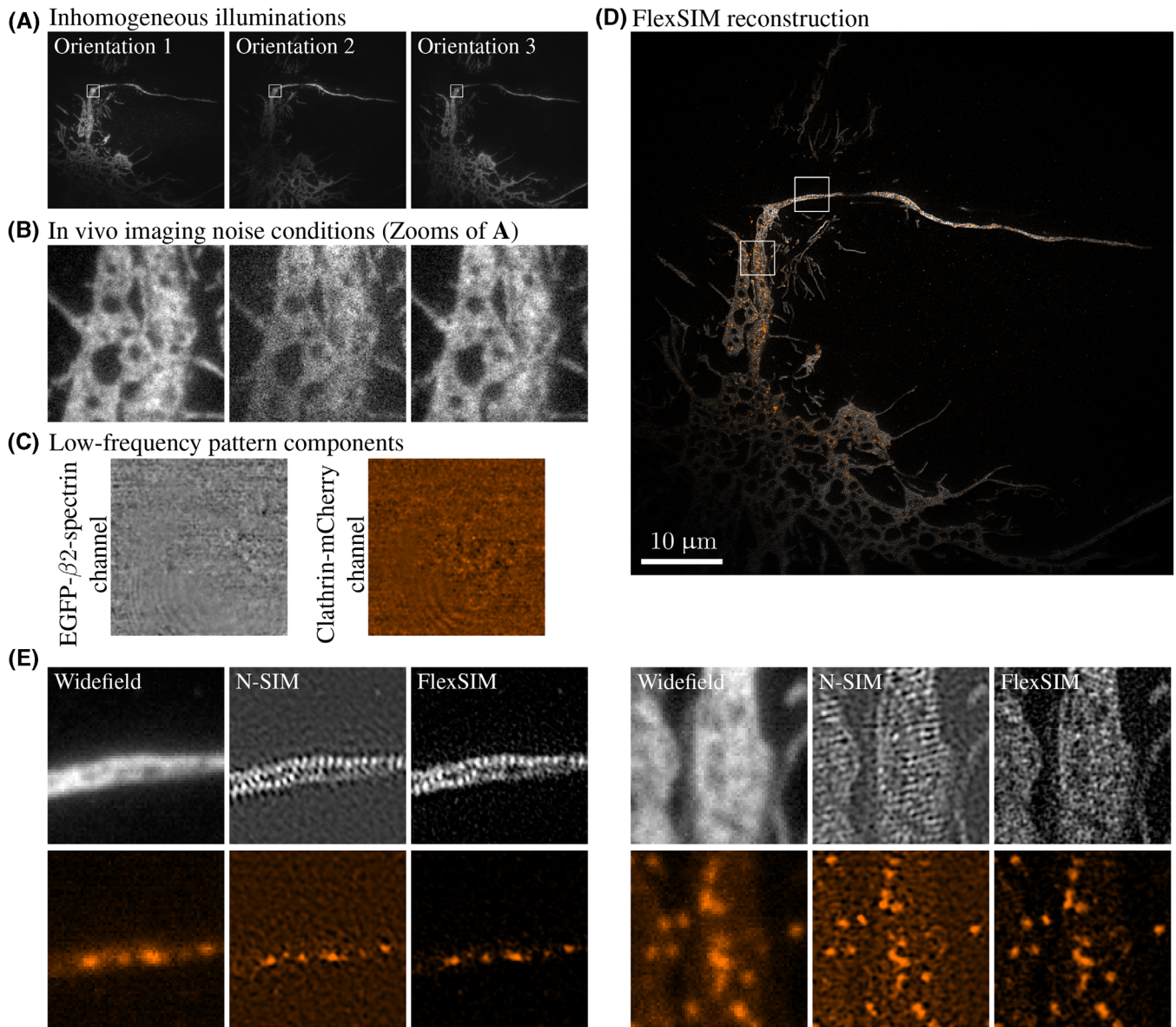


FIGURE 3 FlexSIM in live TIRF-SIM imaging conditions. Clathrin-mCherry (orange) and EGFP-β2-spectrin expressed by a living neuron (grey). An 18-frame acquisition is performed with the Nikon N-SIM-S system in TIRF-SIM mode. Raw images are of size (1024×1024) and reconstructions are (2048×2048) . (A) Raw SIM data exhibit inhomogeneous illumination as well as (B) high noise levels. (C) Low-frequency pattern component estimated by FlexSIM. (D) FlexSIM reconstruction (the full temporal stack available in Video S1). (E) Zooms for the comparison of FlexSIM and N-SIM reconstructions.

The FlexSIM reconstruction module is implemented within the GlobalBioIm framework.⁵⁶ As such, a variety of regularisers \mathcal{R} and optimisation algorithms to solve (8) are available. By default, first-order Tikhonov, smoothed total-variation⁶⁹ and good-roughness⁷⁰ regularisers are proposed in FlexSIM. They all lead to a differentiable objective function in (8) that can be minimised through the second-order variable-metric limited-memory-bounded algorithm⁷¹ belonging to the family of L-BFGS methods. For all the experiments reported in this work, we considered the first-order Tikhonov regulariser which leads to faster computation and always provided very sat-

isfactory results even with challenging data. We attribute the fact that such a simple regulariser is sufficient to the redundancy that exists in the 9 SIM raw images.⁷² Indeed, this redundancy reduces the impact of using more sophisticated regularisers.

2.3.3 | Weighted L_2 -norm

In FlexSIM, we exploit the weighted L_2 data-fidelity term $\|\cdot\|_{M_p}^2$ to account for both Poisson noise and out-of-focus fluorescence.

Poisson noise. As in any fluorescence microscopy system, the noise in the raw SIM data is a mix of Gaussian (e.g., readout noise) and Poisson (photon-counting process of the detectors) noise. Because the associated log-likelihood is very challenging to optimise,⁷³ standard practice is to adopt the simplifying assumption that the overall noise is a nonstationary uncorrelated Gaussian noise. This can be achieved by setting $\mathbf{M}_p = \mathbf{diag}(\mathbf{1}/(\mathbf{y}_p + \sigma^2))$ (component-wise division), where σ^2 corresponds to the variance of the Gaussian part of the noise.^{67,74}

Out-of-focus fluorescence. Out-of-focus fluorescence can be a source of severe reconstruction artefacts.^{40,41} To address this issue, reconstruction approaches that explicitly model and estimate the background signal have been proposed.^{47–49} Another very common strategy is known as OTF attenuation.⁵⁹ It proceeds by attenuating the central frequencies of the OTF used in the Wiener-based final reconstruction. Basically, this is achieved through a pointwise multiplication of the OTF with a function of the form

$$\nu(\mathbf{k}) = 1 - \alpha \exp(-\|\mathbf{k}\|_2^2 / (2\beta^2)), \quad (9)$$

where $\alpha > 0$ and $\beta > 0$ control the strength and the width of the attenuation, respectively. In this way, the frequency components that do not transmit any information about the missing cone are attenuated, thereby enhancing the components that can instead fill the missing cone (we refer the reader to the very instructive material, i.e., Ref. 59, fig. 7). From a variational viewpoint such as (8), this OTF-attenuation strategy amounts to set $\mathbf{M}_p = \mathbf{H}_{\text{Att}}$, a convolution operator whose kernel is given in Fourier domain by ν in (9). Indeed, with this choice and setting $\mathcal{R} = \|\cdot\|_2^2$ in (8), we recover the standard Wiener-based reconstruction with OTF attenuation. This particular formulation allows us to interpret OTF attenuation as a means of giving more importance to high-frequency errors than to low-frequency errors (including errors due to the background) in the data-fidelity term.

In accordance with this section, we define in FlexSIM the data-fidelity term with \mathbf{M}_p a composition of $\mathbf{diag}(\mathbf{1}/(\mathbf{y}_p + \sigma^2))$ and \mathbf{H}_{Att} .

2.4 | Sample preparation

COS-7 cells were briefly extracted in Triton X-100/glutaraldehyde, then fixed using glutaraldehyde, before being quenched, blocked, and stained with anti-clathrin heavy-chain primary antibodies (polyclonal rabbit ab21679, abcam), revealed with donkey anti-rabbit secondary antibodies conjugated to Alexa Fluor 647 and anti-alpha tubulin primary antibodies (monoclonal

mouse clones B-5-1-2 and DM1a, Sigma), revealed with donkey anti-mouse secondary antibodies conjugated to Alexa Fluor 555. To stain actin, cells were incubated with phalloidin-Atto488 at the end of the staining procedure.⁷⁵

Regarding macrophages imaging (Figure S9), macrophages were transduced with GFP-paxillin lentiviruses (BiVic facility, Toulouse, France) for 3 days as previously described.³⁴ Macrophages were fixed with paraformaldehyde and were placed on a FluoroDish (WPI FD35-100) and immersed in PBS.

2.5 | TIRF-SIM imaging and N-SIM processing

We used a Nikon N-SIM-S microscope to image COS-7 cells stained for actin via classical two-beam TIRF-SIM. Cells were mounted in a Ludin chamber in 0.1M phosphate buffer. The sample was illuminated using a 488 nm laser with 2 opposite beams at the periphery of the back focal plane of a 100 \times , 1.49 NA objective, with 9 images (3 phases \times 3 orientations; 16-bit, (1024 \times 1024) pixels at 65 nm/pixel) captured over a 50 ms exposure time by an Hamamatsu Fusion BT sCMOS camera. The raw images were then processed using the N-SIM module of the NIS Elements software, resulting in a 32-bit, (2048 \times 2048) pixel reconstructed image at 32.5 nm/pixel.

3 | RESULTS

3.1 | FlexSIM deals with pattern distortions

An important feature of FlexSIM lies in its ability to cope with illumination patterns that exhibit a nonuniform low-frequency component, as described in (1). We report in Figure 2 an example of challenging TIRF-SIM data that are affected by such a degradation. Although not clearly visible on individual raw images (Figure S5A), slowly varying concentric rings become apparent if one switches rapidly from one image to the next. The origin of these distortions is not entirely clear. They are most likely due to reflections from the TIRF edge configuration and, to date, cannot be systematically corrected on the optical side. Fortunately, these distortions are captured perfectly by the low-frequency component \underline{w} estimated by FlexSIM (Figures 2B and S5B). Then, by incorporating these into the reconstruction process and by reconstructing each orientation separately, FlexSIM is able to produce well-contrasted and sharp images while standard SIM-reconstructions suffer from strong grid artefacts (Figure 2A). Even the advanced OTF shaping proposed in HiFi-SIM²² fails to avoid grid artefacts

(Figure S6B). In contrast, FlexSIM is able to significantly reduce these artefacts, albeit we can observe that some still remain in localised areas (cf. bottom left border of the cell in Figure 2A). Finally, it is worth mentioning that the grid artefacts reappear on FlexSIM reconstructions if we ignore \underline{w} or if we do not consider each pattern orientation separately (Figure S6A). These complementary experiments strengthen the relevance and importance of the new features proposed in FlexSIM.

We report in Figures S7 and S8 two additional reconstructions over the twelve similar cell samples we acquired on the same TIRF-SIM system. One observes that, when the estimated low-frequency pattern component \underline{w} is homogeneous (clathrin channel in Figure S7C, actin and clathrin channels in Figure S8C), no artefacts are visible in the N-SIM reconstruction as well. This reinforces the fact that the presence of a nonuniform \underline{w} is at the origin of the observed artefacts. Moreover, it is worth mentioning that, even when N-SIM reconstructions do not present artefacts, the corresponding FlexSIM reconstructions exhibit better contrast and dynamics.

3.2 | FlexSIM copes with difficult live imaging conditions

The TIRF-SIM data of Figure 2, which are already quite challenging, were acquired in fixed imaging conditions with high photon collection and low noise. In Figure 3, we consider even more challenging data by assessing the performance of FlexSIM in extreme live-imaging conditions. Precisely, we imaged a living neuron transfected with EGFP- β 2-spectrin and clathrin-mCherry.⁷⁶ In addition to the presence of a low-frequency pattern component (Figure 3C), these data present several other difficulties. In particular, they suffer from low photon collection (high noise) and strong illumination inhomogeneities that also vary according to the orientation of the pattern (Figure 3A and B). Additionally, the imaged structure (neuron) only covers a small portion of the field of view. Lastly, β 2-spectrin forms periodic bands spaced by 190 nm along the axon. They are not visible on the widefield image and their spatial frequency is close to that of the grid artefacts.

The FlexSIM reconstruction of a temporal frame is presented in Figure 3D. For comparison, the reconstruction obtained using the N-SIM software is depicted in the zooms of Figure 3E. The full reconstructed temporal stack is provided in Video S1. While both methods are able to reveal the spectrin bands (Figure 3E, left), they appear somehow distorted in one direction in the N-SIM reconstruction. We attribute this to the presence of grid artefacts intermingled with the actual pattern of

the spectrin bands. Such grid artefacts are clearly visible in the proximal axon and dendritic region on the N-SIM reconstruction (Figure 3E, right). Finally, FlexSIM has the remarkable ability to produce reconstructions free from residual background.

We also evaluated the performance of FlexSIM on data collected using a home-built TIRF-SIM system in Figure S9 (live macrophage expressing GFP-paxillin³⁵). To illustrate the difficulty of reconstructing these data, we were unable to estimate the frequencies and phases of patterns using FairSIM.¹⁸ While HiFi-SIM²² performed better for this task, the best reconstruction we managed to obtain with it (or JSFR-SIM²⁴) suffer from important artefacts. In contrast, FlexSIM was able to properly estimate patterns parameters and to provide a clear reconstruction.

3.3 | FlexSIM achieves state-of-the-art performance on a variety of open SIM datasets

To further demonstrate the capabilities of FlexSIM, we conducted in-depth comparisons with existing SIM reconstruction approaches. We considered twenty open 2D-SIM datasets sourced from seven publications and acquired with a diversity of SIM systems and configurations (see Table S2). Then, we benchmarked FlexSIM against methods developed in publications associated with each of these datasets. This represents seven different SIM reconstruction approaches ranging from standard Wiener-based reconstructions (and more advanced variants) all the way to deep-learning techniques. Accordingly, we could tune the parameters of each method as specified by the authors themselves, which ensures a fair comparison.

A representative subset of the comparisons we made with the most recently published reconstruction approaches is presented in Figure 4. Complementary comparisons are provided in Figures S10–S13. One can see that FlexSIM performs as well as the best-in-class HiFi-SIM²² and JSFR-SIM²⁴ methods while outperforming other algorithms. In particular, due to the proposed weighted-least-squares data-fidelity term, including an OTF attenuation strategy, FlexSIM is able to attenuate out-of-focus signal and typical associated artefacts similarly to what is achieved by HiFi-SIM and JSFR-SIM. As with the TIRF-SIM data presented in the previous paragraphs, we can appreciate the ability of FlexSIM to systematically provide well-contrasted and crisp reconstructions across the large variety of data gathered in Table S2. In addition to these extensive experiments on open real data, we report in *Supplementary Note 2* quantitative comparisons on simulated data. These results support the fact that FlexSIM not only handles very difficult data (as demonstrated in

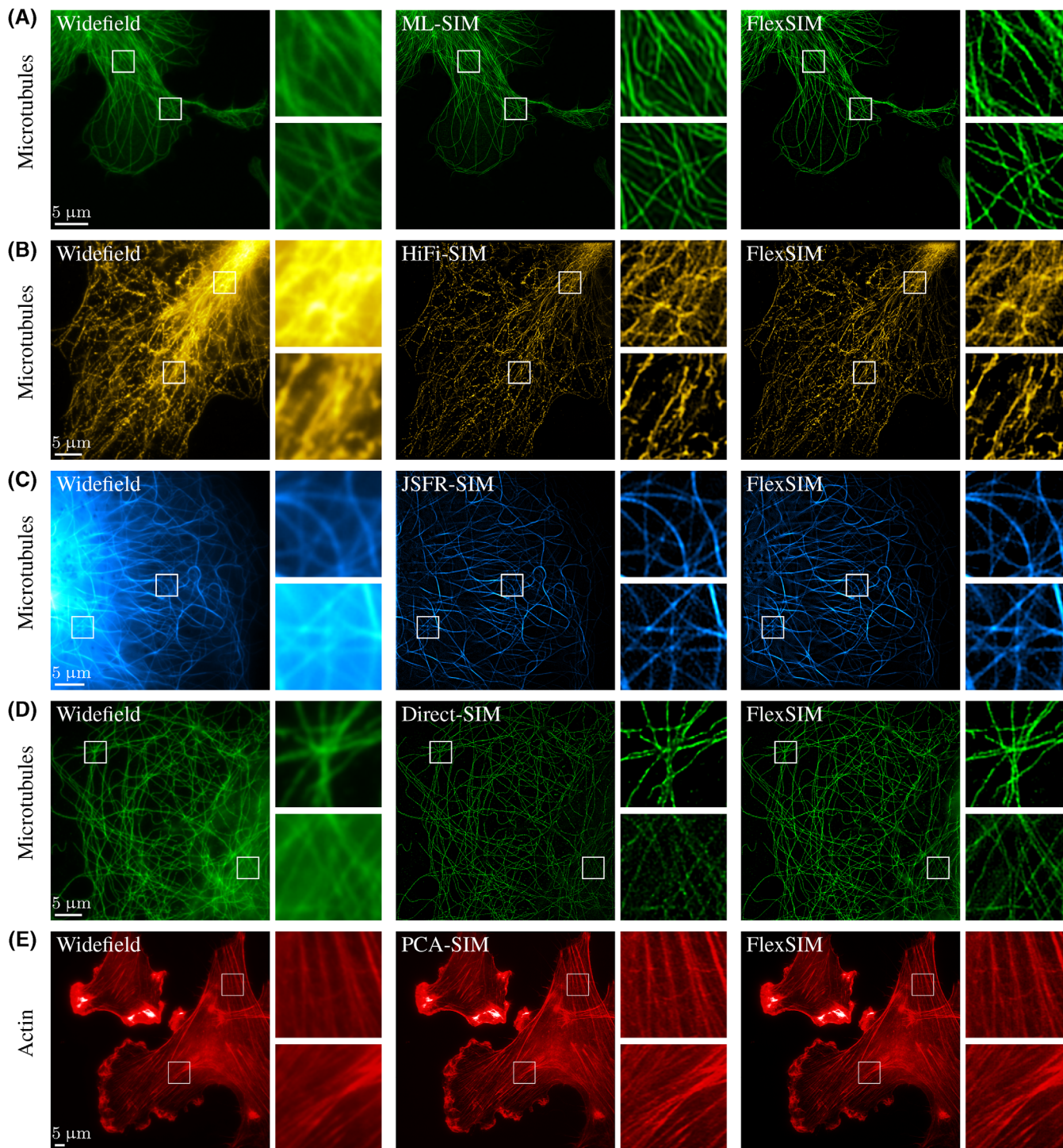


FIGURE 4 Benchmarking FlexSIM against existing software on their own datasets. A subset of the 20 open 2D-SIM datasets reported in Table S2. From left to right, columns correspond to the widefield image, the comparative reconstruction and the FlexSIM reconstruction. Other comparisons are provided in Figures S10–S13. Note that PCA-SIM⁶³ in E is a method that uses principal component analysis for the estimation of patterns parameters. The reconstruction is then performed using HiFi-SIM.²²

previous paragraphs) but also achieves peak performance on more standardised datasets.

Finally, FlexSIM Matlab scripts for each dataset of Table S2 are publically available within the FlexSIM GitHub repository. These scripts automatically download

the raw SIM data and set all FlexSIM parameters used to reproduce the results reported in the present paper for the sake of reproducibility. Beyond allowing us to assess FlexSIM performance, another motivation was to catalogue open 2D-SIM datasets and facilitate their access. We

intend to update and enrich this collection of datasets as new ones are released.

4 | DISCUSSION

We have demonstrated experimentally the flexibility of FlexSIM to cope with a broad range of SIM data. We have included very challenging data for which no published method was known to attenuate the reconstruction artefacts as well as FlexSIM. To achieve this, we equipped FlexSIM with advanced features that include the modelling of a class of pattern distortions, the consideration of shot noise, and the attenuation of out-of-focus fluorescence. The price to pay, however, is the need for an iterative reconstruction scheme which is slower than direct Wiener-based inversion. Typically, our reconstruction of the (2048 × 2048) TIRF-SIM images (e.g., Figures 2 and 3) is obtained in about 6 min on a Dell Latitude computer (Intel Core i7-8650U CPU 1.90 GHz × 8) with parallel computing. The reconstruction time for smaller (1024 × 1024) images ranges between 1 and 3 min, depending on the number of iterations. We expect that the computational time of FlexSIM can be markedly decreased if one deploys GPU computation.⁷⁷

We acquired new insights while developing FlexSIM. In particular, the estimation of pattern frequencies and phases through the formalisation of this problem as the minimisation of a suitable criteria helped us to clarify certain assumptions that had remained implicit to this day. This has allowed us to integrate them properly within the problem (see Figure S3). Moreover, we have highlighted the benefit of our local off-the-grid refinement over an oversampling of the data to achieve subpixel wave vector localisation (see Figure S4).

Finally, FlexSIM is available as a documented open-source code with a pool of example scripts that allow one to reproduce the reconstructions reported in this work for each dataset of Table S2. Users can also deploy FlexSIM easily on any other dataset by filling a single file collecting every required parameter.


ACKNOWLEDGEMENTS

The authors thanks Renaud Poincloux from Institut de Pharmacologie et de Biologie Structurale in Toulouse for the preparation of the macrophage podosomes used in Figure S9. C.L. acknowledges the INP NCIS imaging facility and Nikon Center of Excellence for Neuro-NanoImaging for service and expertise.

CONFLICT OF INTEREST STATEMENT

The authors declare no conflicts of interest.

ORCID

Emmanuel Soubies  <https://orcid.org/0000-0003-0571-6983>

REFERENCES

- Heintzmann, R., & Cremer, C. G. (1999). Laterally modulated excitation microscopy: Improvement of resolution by using a diffraction grating. In Proceedings of the SPIE, Optical Biopics and Microscopic Techniques III (Vol. 3568, pp. 185–196). Stockholm, Sweden.
- Gustafsson, M. G. L. (2000). Surpassing the lateral resolution limit by a factor of two using structured illumination microscopy. *Journal of Microscopy*, *198*(2), 82–87.
- Heintzmann, R., & Huser, T. (2017). Super-resolution structured illumination microscopy. *Chemical Reviews*, *117*(23), 13890–13908.
- Wu, Y., & Shroff, H. (2018). Faster, sharper, and deeper: Structured illumination microscopy for biological imaging. *Nature Methods*, *15*(12), 1011–1019.
- Ma, Y., Wen, K., Liu, M., Zheng, J., Chu, K., Smith, Z. J., Liu, L., & Gao, P. (2021). Recent advances in structured illumination microscopy. *Journal of Physics: Photonics*, *3*(2), 024009.
- Samanta, K., & Joseph, J. (2021). An overview of structured illumination microscopy: Recent advances and perspectives. *Journal of Optics*, *23*(12), 123002.
- Prakash, K., Diederich, B., Reichelt, S., Heintzmann, R., & Schermelleh, L. (2021). Super-resolution structured illumination microscopy: Past, present and future. *Philosophical Transactions of the Royal Society A*, *379*(2199), 20200143.
- Schermelleh, L., Heintzmann, R., & Leonhardt, H. (2010). A guide to super-resolution fluorescence microscopy. *Journal of Cell Biology*, *190*(2), 165–175.
- Schermelleh, L., Ferrand, A., Huser, T., Eggeling, C., Sauer, M., Biehlmaier, O., & Drummen, G. P. (2019). Super-resolution microscopy demystified. *Nature Cell Biology*, *21*(1), 72–84.
- Prakash, K., Diederich, B., Heintzmann, R., & Schermelleh, L. (2022). Super-resolution microscopy: A brief history and new avenues. *Philosophical Transactions of the Royal Society A*, *380*(2220), 20210110.
- Kner, P., Chhun, B. B., Griffis, E. R., Winoto, L., & Gustafsson, M. G. (2009). Super-resolution video microscopy of live cells by structured illumination. *Nature Methods*, *6*(5), 339–342.
- Hirvonen, L. M., Wicker, K., Mandula, O., & Heintzmann, R. (2009). Structured illumination microscopy of a living cell. *European Biophysics Journal*, *38*, 807–812.
- Lu-Walther, H. W., Kielhorn, M., Förster, R., Jost, A., Wicker, K., & Heintzmann, R. (2015). FastSIM: a practical implementation of fast structured illumination microscopy. *Methods and Applications in Fluorescence*, *3*(1), 014001.
- Markwirth, A., Lachetta, M., Mönkemöller, V., Heintzmann, R., Hübner, W., Huser, T., & Müller, M. (2019). Video-rate multi-color structured illumination microscopy with simultaneous real-time reconstruction. *Nature Communications*, *10*(1), 4315.
- Ward, E. N., Hecker, L., Christensen, C. N., Lamb, J. R., Lu, M., Mascheroni, L., Chung, C. W., Wang, A., Rowlands, C. J., Schierle, G. S. K., & Kaminski, C. F. (2022). Machine learning assisted interferometric structured illumination microscopy for dynamic biological imaging. *Nature Communications*, *13*(1), 7836.

16. Chen, X., Zhong, S., Hou, Y., Cao, R., Wang, W., Li, D., Dai, Q., Kim, D., & Xi, P. (2023). Superresolution structured illumination microscopy reconstruction algorithms: A review. *Light: Science & Applications*, *12*(1), 172.
17. Křížek, P., Lukeš, T., Ovesný, M., Fliegel, K., & Hagen, G. M. (2015). SIMToolbox: A MATLAB toolbox for structured illumination fluorescence microscopy. *Bioinformatics*, *32*(2), 318–320.
18. Müller, M., Mönkemöller, V., Hennig, S., Hübner, W., & Huser, T. (2016). Open-source image reconstruction of super-resolution structured illumination microscopy data in ImageJ. *Nature Communications*, *7*(1), 10980.
19. Lal, A., Shan, C., & Xi, P. (2016). Structured illumination microscopy image reconstruction algorithm. *IEEE Journal of Selected Topics in Quantum Electronics*, *22*(4), 50–63.
20. Huang, X., Fan, J., Li, L., Liu, H., Wu, R., Wu, Y., Wei, L., Mao, H., Lal, A., Xi, P., Tang, L., Zhang, Y., Liu, Y., Tan, S., & Chen, L. (2018). Fast, long-term, super-resolution imaging with Hessian structured illumination microscopy. *Nature Biotechnology*, *36*(5), 451–459.
21. Jin, L., Liu, B., Zhao, F., Hahn, S., Dong, B., Song, R., Elston, T. C., Xu, Y., & Hahn, K. M. (2020). Deep learning enables structured illumination microscopy with low light levels and enhanced speed. *Nature Communications*, *11*(1), 1934.
22. Wen, G., Li, S., Wang, L., Chen, X., Sun, Z., Liang, Y., Jin, X., Xing, Y., Jiu, Y., Tang, Y., & Li, H. (2021). High-fidelity structured illumination microscopy by point-spread-function engineering. *Light: Science & Applications*, *10*(1), 70.
23. Christensen, C. N., Ward, E. N., Lu, M., Lio, P., & Kaminski, C. F. (2021). ML-SIM: Universal reconstruction of structured illumination microscopy images using transfer learning. *Biomedical Optics Express*, *12*(5), 2720–2733.
24. Wang, Z., Zhao, T., Hao, H., Cai, Y., Feng, K., Yun, X., Liang, Y., Wang, S., Sun, Y., Bianco, P. R., Oh, K., & Lei, M. (2022). High-speed image reconstruction for optically sectioned, super-resolution structured illumination microscopy. *Advanced Photonics*, *4*(2), 026003.
25. Wen, G., Li, S., Liang, Y., Wang, L., Zhang, J., Chen, X., Jin, X., Chen, C., Tang, Y., & Li, H. (2023). Spectrum-optimized direct image reconstruction of super-resolution structured illumination microscopy. *Photonix*, *4*(1), 1–18.
26. Qiao, C., Li, D., Liu, Y., Zhang, S., Liu, K., Liu, C., Guo, Y., Jiang, T., Fang, C., Li, N., He, K., Zhu, X., Lippincott-Schwartz, J., Dai, Q., & Li, D. (2023). Rationalized deep learning super-resolution microscopy for sustained live imaging of rapid subcellular processes. *Nature Biotechnology*, *41*(3), 367–377.
27. Cao, R., Li, Y., Chen, X., Ge, X., Li, M., Guan, M., Hou, Y., Fu, Y., Xu, X., Leterrier, C., Jiang, S., Gao, B., & Xi, P. (2023). Open-3DSIM: An open-source three-dimensional structured illumination microscopy reconstruction platform. *Nature Methods*, *20*, 1–4.
28. Heintzmann, R., Jovin, T. M., & Cremer, C. (2002). Saturated patterned excitation microscopy – A concept for optical resolution improvement. *Journal of the Optical Society of America A*, *19*(8), 1599–1609.
29. Gustafsson, M. G. (2005). Nonlinear structured-illumination microscopy: Wide-field fluorescence imaging with theoretically unlimited resolution. *Proceedings of the National Academy of Sciences*, *102*(37), 13081–13086.
30. Rego, E. H., Shao, L., Macklin, J. J., Winoto, L., Johansson, G. A., Kamps-Hughes, N., Davidson, M. W., & Gustafsson, M. G. (2012). Nonlinear structured-illumination microscopy with a photoswitchable protein reveals cellular structures at 50-nm resolution. *Proceedings of the National Academy of Sciences*, *109*(3), E135–E143.
31. Li, D., Shao, L., Chen, B. C., Zhang, X., Zhang, M., Moses, B., Milkie, D. E., Beach, J. R., Hammer, J. A., Pasham, M., Kirchhausen, T., Baird, M. A., Davidson, M. W., Xu, P., & Betzig, E. (2015). Extended-resolution structured illumination imaging of endocytic and cytoskeletal dynamics. *Science*, *349*(6251), aab3500.
32. Mudry, E., Belkebir, K., Girard, J., Savatier, J., Le Moal, E., Nicoletti, C., Allain, M., & Sentenac, A. (2012). Structured illumination microscopy using unknown speckle patterns. *Nature Photonics*, *6*(5), 312–315.
33. Idier, J., Labouesse, S., Allain, M., Liu, P., Bourguignon, S., & Sentenac, A. (2018). On the superresolution capacity of imagers using unknown speckle illuminations. *IEEE Transactions on Computational Imaging*, *4*(1), 87–98.
34. Mangeat, T., Labouesse, S., Allain, M., Negash, A., Martin, E., Guénolé, A., Poincloux, R., Estibal, C., Bouissou, A., Cantaloube, S., Vega, E., Li, T., Rouvière, C., Allart, S., Keller, D., Debarnot, V., Wang, X. B., Michaux, G., Pinot, M., ... Sentenac, A. (2021). Super-resolved live-cell imaging using random illumination microscopy. *Cell Reports Methods*, *1*(1), 100009.
35. Affannoukoué, K., Labouesse, S., Maire, G., Gallais, L., Savatier, J., Allain, M., Rasedujaman, M., Legoff, L., Idier, J., Poincloux, R., Pelletier, F., Leterrier, C., Mangeat, T., & Sentenac, A. (2023). Super-resolved total internal reflection fluorescence microscopy using random illuminations. *Optica*, *10*(8), 1009–1017.
36. Cragg, G. E., & So, P. T. (2000). Lateral resolution enhancement with standing evanescent waves. *Optics Letters*, *25*(1), 46–48.
37. Fiolka, R., Beck, M., & Stemmer, A. (2008). Structured illumination in total internal reflection fluorescence microscopy using a spatial light modulator. *Optics Letters*, *33*(14), 1629–1631.
38. Roth, J., Mehl, J., & Rohrbach, A. (2020). Fast TIRF-SIM imaging of dynamic, low-fluorescent biological samples. *Biomedical Optics Express*, *11*(7), 4008–4026.
39. Guo, Y., Li, D., Zhang, S., Yang, Y., Liu, J. J., Wang, X., Liu, C., Milkie, D. E., Moore, R. P., Tulu, U. S., Kiehart, D. P., Hu, J., Lippincott-Schwartz, J., Betzig, E., & Li, D. (2018). Visualizing intracellular organelle and cytoskeletal interactions at nanoscale resolution on millisecond timescales. *Cell*, *175*(5), 1430–1442.e17.
40. Demmerle, J., Innocent, C., North, A. J., Ball, G., Müller, M., Miron, E., Matsuda, A., Dobbie, I. M., Markaki, Y., & Schermelleh, L. (2017). Strategic and practical guidelines for successful structured illumination microscopy. *Nature Protocols*, *12*(5), 988–1010.
41. Karras, C., Smedh, M., Förster, R., Deschout, H., Fernandez-Rodriguez, J., & Heintzmann, R. (2019). Successful optimization of reconstruction parameters in structured illumination microscopy – A practical guide. *Optics Communications*, *436*, 69–75.
42. Fan, J., Huang, X., Li, L., Tan, S., & Chen, L. (2019). A protocol for structured illumination microscopy with minimal reconstruction artifacts. *Biophysics Reports*, *5*, 80–90.
43. Kraus, F., Miron, E., Demmerle, J., Chitiashvili, T., Budco, A., Alle, Q., Matsuda, A., Leonhardt, H., Schermelleh, L.,

- & Markaki, Y. (2017). Quantitative 3D structured illumination microscopy of nuclear structures. *Nature Protocols*, *12*(5), 1011–1028.
44. Young, L. J., Ströhl, F., & Kaminski, C. F. (2016). A guide to structured illumination TIRF microscopy at high speed with multiple colors. *JoVE (Journal of Visualized Experiments)*, (111), e53988.
 45. Ball, G., Demmerle, J., Kaufmann, R., Davis, I., Dobbie, I. M., & Schermelleh, L. (2015). SIMcheck: A toolbox for successful super-resolution structured illumination microscopy. *Scientific Reports*, *5*(1), 15915.
 46. Wang, Z., Zhao, T., Cai, Y., Zhang, J., Hao, H., Liang, Y., Wang, S., Sun, Y., Chen, T., Bianco, P. R., Oh, K., & Lei, M. (2023). Rapid, artifact-reduced, image reconstruction for super-resolution structured illumination microscopy. *The Innovation*, *4*(3), 100425.
 47. Soubies, E., & Unser, M. (2019). Computational super-sectioning for single-slice structured-illumination microscopy. *IEEE Transactions on Computational Imaging*, *5*(2), 240–250.
 48. Jost, A., Tolstik, E., Feldmann, P., Wicker, K., Sentenac, A., & Heintzmann, R. (2015). Optical sectioning and high resolution in single-slice structured illumination microscopy by thick slice blind-SIM reconstruction. *PLoS One*, *10*(7), e0132174.
 49. Mo, Y., Wang, K., Li, L., Xing, S., Ye, S., Wen, J., Duan, X., Luo, Z., Gou, W., Chen, T., Zhang, Y. H., Guo, C., Fan, J., & Chen, L. (2023). Quantitative structured illumination microscopy via a physical model-based background filtering algorithm reveals actin dynamics. *Nature Communications*, *14*(1), 3089.
 50. Ayuk, R., Giovannini, H., Jost, A., Mudry, E., Girard, J., Mangeat, T., Sandeau, N., Heintzmann, R., Wicker, K., Belkebir, K., & Sentenac, A. (2013). Structured illumination fluorescence microscopy with distorted excitations using a filtered blind-SIM algorithm. *Optics Letters*, *38*(22), 4723–4726.
 51. Labouesse, S., Negash, A., Idier, J., Bourguignon, S., Mangeat, T., Liu, P., Sentenac, A., & Allain, M. (2017). Joint reconstruction strategy for structured illumination microscopy with unknown illuminations. *IEEE Transactions on Image Processing*, *26*(5), 2480–2493.
 52. Xypakis, E., Gosti, G., Giordani, T., Santagati, R., Ruocco, G., & Leonetti, M. (2022). Deep learning for blind structured illumination microscopy. *Scientific Reports*, *12*(1), 8623.
 53. Smith, C. S., Slotman, J. A., Schermelleh, L., Chakrova, N., Hari, S., Vos, Y., Hagen, C. W., Müller, M., van Cappellen, W., Houtsmuller, A. B., Hoogenboom, J. P., & Stallinga, S. (2021). Structured illumination microscopy with noise-controlled image reconstructions. *Nature Methods*, *18*(7), 821–828.
 54. Shah, Z. H., Müller, M., Wang, T. C., Scheidig, P. M., Schneider, A., Schüttelz, M., Huser, T., & Schenck, W. (2021). Deep-learning based denoising and reconstruction of super-resolution structured illumination microscopy images. *Photonics Research*, *9*(5), B168–B181.
 55. Qiao, C., Zeng, Y., Meng, Q., Chen, X., Chen, H., Jiang, T., Wei, R., Guo, J., Fu, W., Lu, H., Li, D., Wang, Y., Qiao, H., Wu, J., Li, D., & Dai, Q. (2024). Zero-shot learning enables instant denoising and super-resolution in optical fluorescence microscopy. *Nature Communications*, *15*(1), 4180.
 56. Soubies, E., Soulez, F., McCann, M. T., Pham, T. a., Donati, L., Debarre, T., Sage, D., & Unser, M. (2019). Pocket guide to solve inverse problems with GlobalBioIm. *Inverse Problems*, *35*(10), 104006.
 57. Lukeš, T., Hagen, G. M., Křížek, P., Švindrych, Z., Fliegel, K., & Klíma, M. (2014). Comparison of image reconstruction methods for structured illumination microscopy. In *Proceedings of the SPIE 9129 Biophotonics: Photonic Solutions for Better Health Care IV* (pp. 607–619). Brussels, Belgium.
 58. Shroff, S. A., Fienup, J. R., & Williams, D. R. (2009). Phase-shift estimation in sinusoidally illuminated images for lateral super-resolution. *Journal of the Optical Society of America A*, *26*(2), 413–424.
 59. Wicker, K., Mandula, O., Best, G., Fiolka, R., & Heintzmann, R. (2013). Phase optimisation for structured illumination microscopy. *Optics Express*, *21*(2), 2032–2049.
 60. Wicker, K. (2013). Non-iterative determination of pattern phase in structured illumination microscopy using auto-correlations in Fourier space. *Optics Express*, *21*(21), 24692–24701.
 61. Cao, R., Chen, Y., Liu, W., Zhu, D., Kuang, C., Xu, Y., & Liu, X. (2018). Inverse matrix based phase estimation algorithm for structured illumination microscopy. *Biomedical Optics Express*, *9*(10), 5037–5051.
 62. Condat, L., Boulanger, J., Pustelnik, N., Sahnoun, S., & Sengmanivong, L. (2014). A 2-D spectral analysis method to estimate the modulation parameters in structured illumination microscopy. In *2014 IEEE 11th International Symposium on Biomedical Imaging (ISBI)* (pp. 604–607). IEEE.
 63. Qian, J., Cao, Y., Bi, Y., Wu, H., Liu, Y., Chen, Q., & Zuo, C. (2023). Structured illumination microscopy based on principal component analysis. *eLight*, *3*(1), 4.
 64. Perez, V., Chang, B. J., & Stelzer, E. H. K. (2016). Optimal 2D-SIM reconstruction by two filtering steps with Richardson-Lucy deconvolution. *Scientific Reports*, *6*(1), 37149.
 65. Lukeš, T., Křížek, P., Švindrych, Z., Benda, J., Ovesný, M., Fliegel, K., Klíma, M., & Hagen, G. M. (2014). Three-dimensional super-resolution structured illumination microscopy with maximum a posteriori probability image estimation. *Optics Express*, *22*(24), 29805–29817.
 66. Orioux, F., Sepulveda, E., Loriette, V., Dubertret, B., & Olivio-Marin, J. C. (2012). Bayesian estimation for optimized structured illumination microscopy. *IEEE Transactions on Image Processing*, *21*(2), 601–614.
 67. Boulanger, J., Pustelnik, N., Condat, L., Sengmanivong, L., & Pilot, T. (2018). Nonsmooth convex optimization for structured illumination microscopy image reconstruction. *Inverse Problems*, *34*(9), 095004.
 68. Zhao, W., Zhao, S., Li, L., Huang, X., Xing, S., Zhang, Y., Qiu, G., Han, Z., Shang, Y., Sun, D. e., Shan, C., Wu, R., Gu, L., Zhang, S., Chen, R., Xiao, J., Mo, Y., Wang, J., Ji, W., ... Chen, L. (2022). Sparse deconvolution improves the resolution of live-cell super-resolution fluorescence microscopy. *Nature Biotechnology*, *40*(4), 606–617.
 69. Aujol, J. F. (2009). Some first-order algorithms for total variation based image restoration. *Journal of Mathematical Imaging and Vision*, *34*, 307–327.
 70. Verveer, P. J., Gemkow, M. J., & Jovin, T. M. (1999). A comparison of image restoration approaches applied to three-dimensional confocal and wide-field fluorescence microscopy. *Journal of Microscopy*, *193*(1), 50–61.

71. Thiébaud, E. (2002). Optimization issues in blind deconvolution algorithms. In Proceedings of the SPIE 4847, Astronomical Data Analysis II (pp. 174–183). Waikoloa, Hawaii, United States.
72. Heintzmann, R. (2003). Saturated patterned excitation microscopy with two-dimensional excitation patterns. *Micron*, 34(6), 283–291. Super-Resolution.
73. Chouzenoux, E., Jezierska, A., Pesquet, J. C., & Talbot, H. (2015). A convex approach for image restoration with exact Poisson–Gaussian likelihood. *SIAM Journal on Imaging Sciences*, 8(4), 2662–2682.
74. Soulez, F. (2014). A “learn 2D, apply 3D” method for 3D deconvolution microscopy. In 2014 IEEE 11th International Symposium on Biomedical Imaging (ISBI) (pp. 1075–1078). IEEE.
75. Jimenez, A., Friedl, K., & Leterrier, C. (2020). About samples, giving examples: Optimized single molecule localization microscopy. *Methods*, 174, 100–114.
76. Wernert, F., Moparthy, S. B., Lainé, J., Moulay, G., Boroni-Rueda, F., Pelletier, F., Jullien, N., Benkhalifa-Ziyat, S., Papandreou, M. J., Leterrier, C., & Vassilopoulos, S. (2023). The actin-spectrin submembrane scaffold restricts endocytosis along proximal axons. *bioRxiv*.
77. Oh, K., & Bianco, P. R. (2023). High-speed image reconstruction for super-resolution structured illumination microscopy using

facile optimization and conversion of reconstruction code in the GPU environment. In SPIE-CLP Conference on Advanced Photonics 2023 (Vol. 12746, pp. 12–19). San Diego, California, United States.

SUPPORTING INFORMATION

Additional supporting information can be found online in the Supporting Information section at the end of this article.

How to cite this article: Soubies, E., Nogueron, A., Pelletier, F., Mangeat, T., Leterrier, C., Unser, M., & Sage, D. (2024). Surpassing light inhomogeneities in structured-illumination microscopy with FlexSIM. *Journal of Microscopy*, 1–13. <https://doi.org/10.1111/jmi.13344>